Check for updates

# Cisplatin delivery, anticancer and antibacterial properties of Fe/SBA-16/ZIF-8 nanocomposite†

Rabindran Jermy Balasamy, [iD] *[a] Vijaya Ravinayagam,*[b] Munther Alomari,[c] Mohammad Azam Ansari,[d] Sarah Ameen Almofty,[c] Suriya Rehman,[d] Hatim Dafalla,[e] Palanivel Rubavathi Marimuthu,[f] Sultan Akhtar [iD] [g] and Mohammad Al Hamad [iD] [h]

Nanoformulation involving biocompatible MOFs and magnetic nanocarriers is an emerging multifunctional platform for drug delivery and tumor imaging in targeted cancer therapeutics. In this study, a nanocomposite has been developed comprising Fe/SBA-16 and ZIF-8 (Fe/S-16/ZIF-8) through ultrasonication. The drug delivery of cisplatin was studied using an automated diffusion cell system equipped with a flow type Franz cell. The anticancer activity of Fe/S-16/ZIF-8 was studied *in vitro* in MCF-7, HeLa cells and Human Foreskin Fibroblast (HFF-1) cells. XRD and $d$-spacing measurements of Fe/S-16/ZIF-8 using TEM revealed the presence of cubic-structured $Fe_3O_4$, $\gamma$-$Fe_2O_3$ (magnetite), and $\alpha$-FeOOH (goethite) over an SBA-16/ZIF-8 nanocomposite. The composite showed a surface area of 365 $m^2$ $g^{-1}$, a pore size of 8.3 nm and a pore volume of 0.33 $cm^3$ $g^{-1}$. VSM analysis of Fe/S-16/ZIF-8 showed that it possessed paramagnetic behavior with a saturated magnetization value of 2.39 emu $g^{-1}$. The $Fe^{2+}$/$Fe^{3+}$ coordination environment was characterized using diffuse reflectance spectroscopy. The cisplatin drug delivery study clearly showed the synergistic effects present in Fe/S-16/ZIF-8 with over 75% of cisplatin release as compared to that of Fe/S-16 and ZIF-8, which showed 56% and 7.5%, respectively. The morphology analysis of CP/Fe/SBA-16/ZIF-8 using TEM showed an effective transit of nanoparticles into MCF-7 cells. The lethal concentration ($LC_{50}$) of Fe/SBA-16/ZIF-8 for MCF-7 and HeLa cells is 0.119 mg $mL^{-1}$ and 0.028 mg $mL^{-1}$ at 24 h, respectively. For HFF-1 cells, the $LC_{50}$ is 0.016 mg $mL^{-1}$. The antibiofilm activity of Fe/SBA-16/ZIF-8 was investigated against biofilm-forming strains of drug resistant *P. aeruginosa* and MRSA by a microtiter tissue culture plate assay. Overall, nanosized ZIF-8 with a bioactive alkaloid imidazole inside the 3D cage type of SBA-16 pores is found to exhibit both anticancer and antibacterial properties. A Fe/S-16/ZIF-8 composite could be effectively used as a drug and drug delivery system against cancer and promote antibacterial activity.

*[a]Department of Nano-Medicine Research, Institute for Research and Medical Consultations, Imam Abdulrahman Bin Faisal University, Dammam, Saudi Arabia. E-mail: rjermy@iau.edu.sa; Tel: +966 3330881*

*[b]Deanship of Scientific Research, Department of Nano-Medicine Research, Imam Abdulrahman Bin Faisal University, Dammam, Saudi Arabia. E-mail: vrnayagam@iau.edu.sa*

*[c]Department of Stem Cell Biology, Institute for Research and Medical Consultations, Imam Abdulrahman Bin Faisal University, Dammam, Saudi Arabia*

*[d]Department of Epidemic Diseases Research, Institute for Research and Medical Consultations (IRMC), Imam Abdulrahman Bin Faisal University, P. O. Box 1982, Dammam 31441, Saudi Arabia*

*[e]College of Engineering Research (CER), King Fahd University of Petroleum and Minerals, 31261, Dhahran, Saudi Arabia*

*[f]Deanship of Quality and Academic Accreditation, Imam Abdulrahman Bin Faisal University, Post Box No. 1982, Dammam 31441, Saudi Arabia*

*[g]Department of Biophysics Research, Institute for Research and Medical Consultations, Imam Abdulrahman Bin Faisal University, P. O. Box. 1982, Dammam 31441, Saudi Arabia*

*[h]Department of Pathology, College of Medicine, Imam Abdulrahman Bin Faisal University, Post Box No. 1982, Dammam 31441, Saudi Arabia*

† Electronic supplementary information (ESI) available. See DOI: 10.1039/c9ra07461a

## 1. Introduction

Metal–organic frameworks (MOFs) are interesting porous crystalline materials that have been recently reported for biomedical applications.[1,2] MOFs with biocompatible metal ions (iron) and bioactive linkers (nicotinic acid) have been reported to be the most suitable for drug delivery through their hybrid composition disintegration under physiological conditions.[3] A MOF system with the ability to act as a photosensitizer, containing ZnO as the gate keeper in the porphyrinic-based MOF with a nucleolin-based AS1411 aptamer, showed that doxorubicin can be efficiently delivered *via* photodynamic-chemo therapy.[4] An efficient loading of 6-mercaptopurine (anti-leukemia drug) over ZIF-8 was reported to deliver the drug over 7 days within the acidic tumor environment at pH 5.[5] Zeolitic imidazolate frameworks (ZIFs) are a new type of metal–organic frameworks (MOFs) built with metal ions ($M^{2+}$) and imidazolate linkers.[6] The porous ZIFs mimic the stable aluminosilicate zeolite structure, where the

metal ion and imidazolate anions play the role of silicon and oxygen, respectively. Compared to conventional MOFs, ZIFs exhibit high chemical resistivity and robust thermal and chemical stability. However, a number of ZIFs are microporous in nature, which limits their applications in bioimaging and drug delivery.[7] In recent years, various techniques have been applied to prepare composites involving ZIF-8 and mesostructured materials. Such composites are most effective because they combine the advantages of microporous ZIF-8 and mesoporous materials. Hybrids involving ZIF-8 with mesoporous MCM-41 (Mobil Composition of Matter no. 41), SBA-15 (Santa Barbara Amorphous no. 15) and UVM-7 (University of Valencia Materials-7) have been reported to demonstrate efficient adsorptive desulfurization compared to pure forms of mesoporous materials and ZIF-8.[8,9] Gold nanoparticles integrated into the mesoporous silica and ZIF-8 crystal have been shown to form unique functional systems with an enhanced plasmonic effect and sieving capabilities for molecular identification.[10] Wang *et al.*[11] described the preparation of Cu–MOF/mesoporous carbon composites using a one-pot synthesis process. Engineered composites have been shown to exhibit desirable electrocatalytic processes for the potential development of electrodes. Zhang *et al.*[12] reported the preparation of palladium-deposited composites involving spherical silica with ZIF-8. The formation of a ZIF-8 shell over a spherical shaped silica core tends to form a hierarchical structure and exhibit high catalytic activity in the hydrogenation of hexenes (1-hexene and cyclohexene). A 10 and 20 wt% of ZIF-8 to silica aerogel composite prepared through a sol–gel technique exhibited a high surface area ranging between 540–563 $m^2 g^{-1}$ and tunable pores between 2.87–3.03 nm.[13]

Cisplatin (*cis*-diamminedichloroplatinum(II)) is a platinum-based chemomedicine used for different types of cancer. The drug also imposes several side effects related to the dose and renal toxicity.[14] However, the beneficial cytotoxic effect of cisplatin can be effectively utilized using several nanocarriers.[15,16] In the present study, cisplatin release at the acidic pH conditions of tumors and the anticancer and antibacterial activity of ZIF-8 was studied using a Fe/SBA-16/ZIF-8 nanoformulation. 10 wt% superparamagnetic iron oxide nanoparticles (SPIONs) were impregnated with mesoporous SBA-16, and then loaded with ZIF-8 (~13 mg). The developed SPIONs/SBA-16/ZIF-8 composite was then functionalized with cisplatin (~30 mg). The presence of a high surface area 3D cubic pore architecture with magnetic behavior is proposed to reduce the SPION aggregation and ZIF-8 toxicity. In this study, drug release was studied using a continuous flow system (open) that mimics *in vitro* drug release. Unlike conventional dialysis membrane techniques (closed system), the sink condition was reduced and saturation was avoided due to the continuous flow of a PBS solution. The sampling error was avoided due to the semi-automated apparatus. The study showed that the imidazole linker present in ZIF-8 itself has an anticancer effect and exhibits high cisplatin drug release capabilities for magnetic field-guided targeted anticancer treatment in *in vitro* cancer cell lines, MCF-7 and HeLa. The antibacterial and antibiofilm activity over Fe/S-16/ZIF-8 was found to be effective when tested against methicillin-resistant *Staphylococcus aureus* (MRSA) and *P. aeruginosa*.

## 2. Methods

### 2.1. Preparation of Fe/SBA-16/ZIF-8

Firstly, nanosupport SBA-16 was prepared by dissolving the non-ionic surfactant F127 (6 g) in an acidic pH solution. Co-surfactant *n*-butanol (19.2 g) and the silica source, tetraethyl orthosilicate (29 g), were then added and stirred vigorously for 24 h. The gel composition was $1TEOS/0.91HCl/119H_2O/0.00344F127$. The milky solution was hydrothermally heated (100 °C, 24 h), filtered, dried and calcined (550 °C, 6 h). 10 wt% iron oxide was then loaded through a wet impregnation technique and then calcined at 550 °C for 2 h. 120 mg of Fe/SBA-16 was taken and dissolved in 15 mL of methanol and stirred for dissolution, after that 12.6 mg of ZIF-8 was added and sonicated for 10 min. Following this, the solution composite was centrifuged and collected. The loaded formulation was labelled as Fe/S-16/ZIF-8.

### 2.2. Preparation of CP/Fe/S-16/ZIF-8

For cisplatin loading, 30 mg of Cp in 10 mL of saline solution was mixed with 600 mg of Fe/SBA-16/ZIF-8 by stirring overnight in the dark on ice. After that, the solution mixture was filtered using a Buchner funnel with sintered disc (G4, 80 mL), and further washed with 15 mL of normal saline solution, and dried at room temperature. Then, the adsorbed cisplatin (0.12 mmol $g^{-1}$ of Fe/S-16/ZIF-8) was calculated using UV-visible spectroscopy at 208 nm.

### 2.3. *In vitro* cisplatin release experiments

The cisplatin release study using different nanoformulations (Fe/MSU-F, Fe/MSU-F-NH$_2$, mesobeta, mesocarbon and Fe/S-16/ZIF-8) was carried out using an assembled Franz cell system (PermeGear, USA). The study in an automated system could define the suitability of cisplatin drug release and analyze the quality and reproducibility of the nanoformulations. The instrument consists of different compartments, including solvent reservoir (PBS), in-line cells, a peristaltic pump, solution sample collector, and constant water heater circulators (Scheme 1). The instrument works under the continuous liquid flow technique with the temperature of the cells maintained at 37 °C using a JULABO GmbH water bath. Before experiments, the system was sufficiently purged to clear any bubbles. The activated cellulose membrane dialysis tubing (pore size ~ 25 Å, average flat width of 43 mm, MWCO = 14 000) was positioned inside the cell chambers. In the donor region, a mixture of nanoformulation and PBS (30 mg mL$^{-1}$) was placed. Then, a PBS solution at pH 5.6 in the reservoir was continuously pumped using a peristaltic pump at the volume to time ratio of 0.167 (10 mL h$^{-1}$) to the in-line cells. The sample collections (1–6 h) were performed at the interval period of 1 h using vials and analyzed using UV-visible spectroscopy (JASCO). All the experiments were carried out in triplicate.

The cumulative cisplatin release for the period ranging between 0.5–72 h was studied using the conventional dialysis membrane technique. Three nanoformulations involving Fe/S-16, ZIF-8 and Fe/S-16/ZIF-8 were studied. The cellulose membrane dialysis tubing was activated, and drug delivery was

performed by immersing the bag containing 30 mg of drug formulations in 50 mL of phosphate buffered saline (PBS) at pH 5.6. The release was performed under a constant temperature at 37 °C. At regular time intervals, a specific volume of solution was removed (10 mL) and analyzed using UV-visible spectroscopy.

## 2.4. Nanomaterial characterization

Phase transformation were analyzed using benchtop X-ray diffraction analysis (Rigaku Multiplex system, Japan). The surface area of the composites was analyzed using the nitrogen adsorption isotherm, ASAP-2020 plus (Micromeritics, USA). The functional groups of ZIF-8 and cisplatin were detected using spectroscopy (PerkinElmer, USA). The saturated magnetization of the Fe/S-16 composite was analyzed using vibrating sample magnetometry (LDJ Electronics Inc. 9600). The iron oxide coordination environment was measured using diffuse reflectance spectroscopy (V-750, JASCO, Japan). The surface features of different structured silicas were analyzed by scanning electron microscopy (JSM-6610LV from JEOL) and transmission electron microscopy (JEM2100F from JEOL).

The textural features of CP/Fe/S-16/ZIF-8 treated MCF-7 cells were analyzed using TEM microscopy (FEI, Morgagni 268, Czech Republic) at 80 kV. Prior to analysis, the treated sample was made into pellets through centrifugation, followed by washing thoroughly using a glutaraldehyde and paraformaldehyde mixture. After secondary fixation using $OsO_4$ on cells, they were dehydrated using absolute ethanol solution. After embedding cells with a resin mixture, they were cured in an oven (60–70 °C) for 2 days. Then, the specimen was prepared as an ultrathin specimen by sectioning in ultramicrotomy. The specimen after loading onto TEM grids was stained with uranyl acetate to further enhance the contrast of the micrographs.

## 2.5. Cell culture

MCF-7 (breast cancer cell line), HeLa (cervical cancer cell line) and non-cancerous cell human foreskin fibroblast (HFF-1)

(ATCC® SCRC-1041™) were used. The MCF-7 cell line was obtained from Dr Khaldoon M. Alsamman, Clinical Laboratory Science, College of Applied Medical Science, Imam Abdulrahman Bin Faisal University, Dammam, Saudi Arabia. HeLa was purchased from ATCC (ATCC® CCL-2™). A 75 $cm^2$ culture flask was used to grow the cells in RPMI medium supplemented with fetal calf serum (10%) (HyClone, GE Healthcare, Chicago, USA) and penicillin/streptomycin (1%) (Thermo Fisher, Waltham, USA) at 37 °C in a humidified incubator (Heracell 150i, Thermo Scientific, Waltham, MA) with 5% $CO_2$. The cells were cultured in a 96 well plate (Thermo Fisher, Waltham, USA) with $1 \times 10^4$ cells per well. At 80% confluency of cells, varied concentrations of nanoformulated drugs were applied along with the control. After 24 h, the cells were tested for cell survival using the MTT assay, a dye reduction test.

## 2.6. MTT assay

MTT ((3-(4,5-dimethylthiazol-2-yl)-2,5-diphenyltetrazolium bromide), 20 µL (10 mg $mL^{-1}$)) was added over the cultured cells in each well of the 96 well plate. The cells were incubated for 4 h at 37 °C, and then washed to remove the dye using 1× PBS. MTT solvent (150 µL) was used to solubilize the formed formazan dye on the plate shaker (15 min). At 590 nm, the color intensity of the solubilized dye was measured using a multiplate reader (Tecan Infinite® 200 PRO, Switzerland). The intensity of color was calculated and compared with the control and the results were presented as the percentage of cell survival.

## 2.7. Hoechst staining

The cell viability of the treated and control cells was tested by Hoechst staining (Sigma Aldrich). Pre-treated MCF-7 and HFF-1 cells with cisplatin (Cp), 10 wt% SPIONs/S-16-A-Cp, and 10 wt% SPIONs/S-16-AP-Cp or vehicle control were washed with 1× PBS, fixed with ice cold methanol for 5 min and stained with Hoechst (Sigma Aldrich) for 10 min in the dark. Cells were washed again with 1× PBS, dried and mounted with ProLong® Gold Antifade
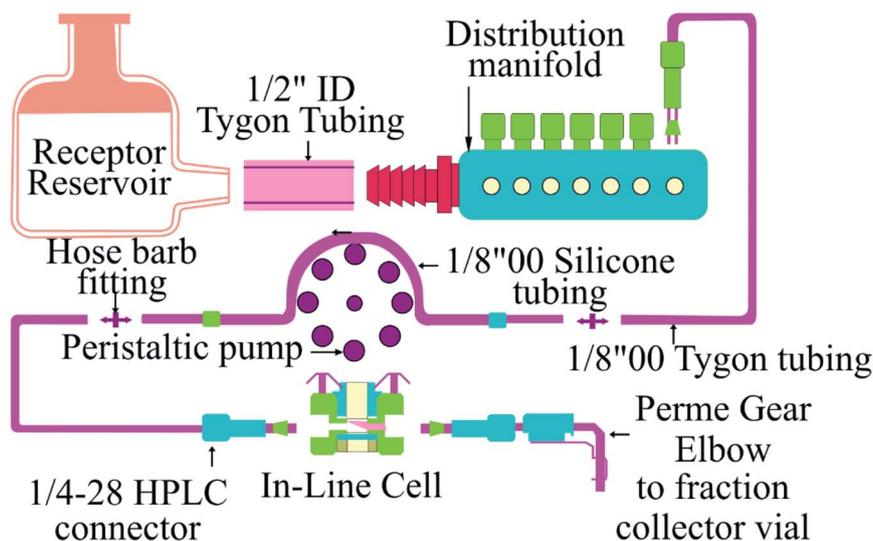


**Scheme 1** Schematic diagram of automated diffusion cell system equipped with flow type Franz cell.

reagent (Thermo Fisher, Waltham, USA). Images were developed with ZEN software using confocal microscopy (Zeiss, Oberkochen, Germany).

### 2.8. Statistical analysis

The *in vitro* cisplatin release statistical differences were analyzed using one-way ANOVA where a *p* value < 0.05 was considered significant.

MTT cell cytotoxicity assay results were subjected to one-way ANOVA followed by Dunnett's *post hoc* test with GraphPad Prism software (GraphPad, La Jolla, CA) on three independent sets of experiments conducted in triplicate. *p* values < 0.05 were considered significant.

### 2.9. Evaluation of antibacterial and antibiofilm activity

**2.9.1. Determination of minimal inhibitory concentration (MIC).** The MIC values of tested compounds against methicillin-resistant *Staphylococcus aureus* (MRSA) and *P. aeruginosa* were determined using a standard two-fold microbroth dilution method.[17] The MIC is defined as the lowest concentration of any compounds and/or agents at which no visible growth of the tested bacteria was observed.

## 3. Biofilm inhibition assay

The antibiofilm potential of tested compounds against *P. aeruginosa* and MRSA biofilms were determined in a sterile 96-well polystyrene (flat bottom) microtiter tissue culture plate as described by Kalishwaralal *et al.*[18] with some modification. Briefly, overnight cultures (20 μL) of tested bacterial strains (1 × $10^7$ CFU mL$^{-1}$) were added in 180 μL of tryptic soy broth containing an increasing concentration of tested compounds (62.5–1000 μg mL$^{-1}$). The microtiter plates were incubated for 18 h at 37 °C. After incubation, the content of each well was discarded and washed two times with 200 μL phosphate buffer saline (PBS) and fixed with 2% sodium acetate and then stained with 0.1% crystal violet solution for 20–30 min. The excess dyes were rinsed off with sterile water and washed again with PBS, and the plates were kept in air to dry. After drying, the stain was solubilized in 200 μL of 95% ethanol and biofilm formation was quantified by measuring the absorbance at $OD_{595}$ and the percent of biofilm inhibition was calculated using the following equation:

$$\% \text{ biofilm inhibition} = \{(\text{OD of control} - \text{OD of tested samples})/(\text{OD of control})\} \times 100$$

## 4. Results and discussion

The cisplatin *in vitro* drug release profile of Fe/MSU-F, Fe/MSU-F-NH$_2$, Mesocarbon, ZIF-8, Mesobeta and Fe/S-16/ZIF-8 was analyzed using an automated Franz cell system. Fig. 1 shows the percentage cumulative release of cisplatin that was repeated thrice over 6 h. The results showed that the Fe/S-16/ZIF-8

nanocomposite exhibited a constant and high cisplatin release of 20% for 6 h. The role of the nanocarrier system is to allow for controlled drug release and reduce the dose release in cancer therapeutics. The release of ZIF-8, Fe/S-16 and Fe/S-16/ZIF-8 for an extended release period over 72 h was studied using a dialysis membrane (Fig. 2). The percentage cumulative release of cisplatin at pH 5 over ZIF-8, Fe/S-16 and Fe/S-16/ZIF-8 is shown in Fig. 2. The study clearly shows the synergistic effect of Fe/S-16/ZIF-8 with over 75% of cisplatin release in comparison to Fe/S-16 and ZIF-8, which showed 56% and 7.5%, respectively. The release profile showed a slow and lower release of cisplatin from ZIF-8 and Fe/S-16 nanocarriers compared to that of Fe/S-16/ZIF-8. Kaur *et al.*[19] reported that at acidic conditions (pH 5) in the tumor, the disintegration of nanosized ZIF-8 occurs and tends to increase the drug release at a faster rate than at a high pH of 7.4. Based on the present objectives of this study, Fe/S-16/ZIF-8 is found to be the optimum carrier as it exhibits a sustained release of cisplatin.
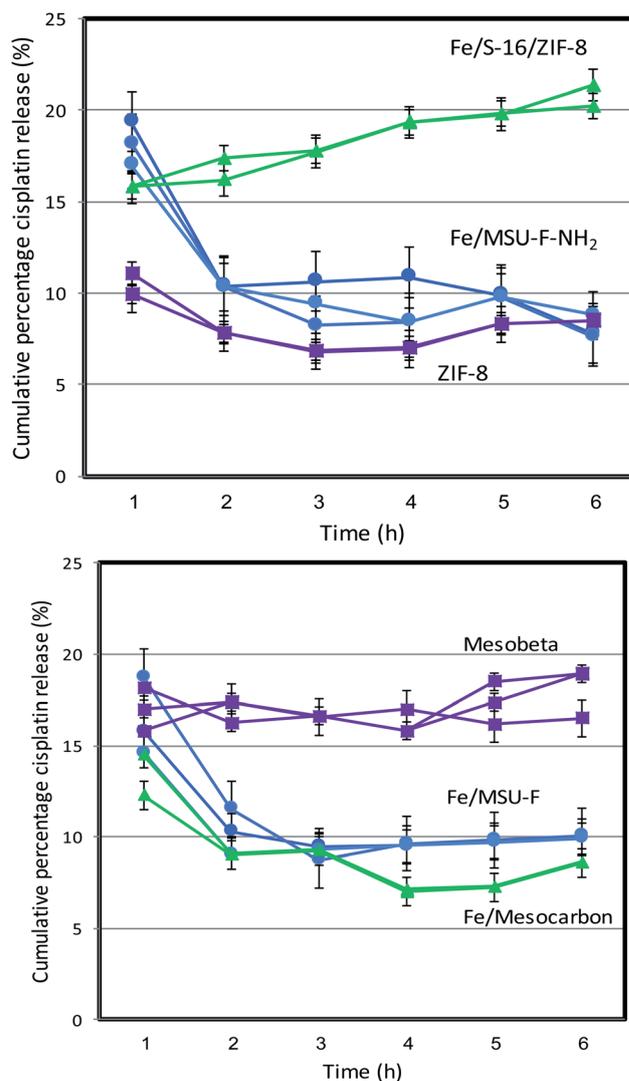


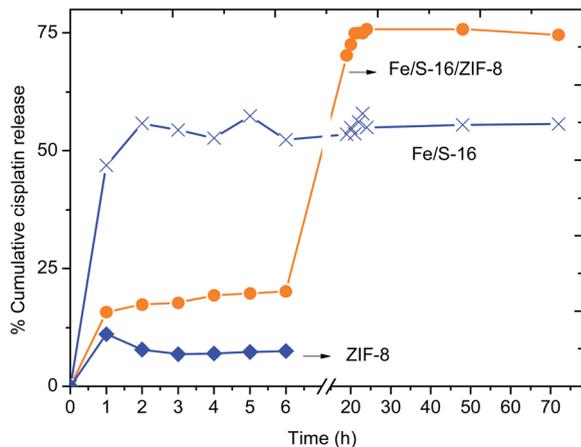**Fig. 1** *In vitro* drug release profile of cisplatin using an automated Franz cell system.

**Fig. 2** Cisplatin drug release of ZIF-8, Fe/S-16 and Fe/S-16/ZIF-8.

In summary, the high cisplatin sustained pH-stimuli drug release was more advantageous with Fe/S-16/ZIF-8 than with Fe/S-16 and ZIF-8. In order to analyze the cisplatin delivery of the developed nanoformulations, one-way ANOVA was applied to six different formulations within each group at interval periods of 1, 2, 3, 4, 5 and 6 h. The results are presented in Table S1.† There were no significant differences observed within the groups indicating that each formulation has exemplary repeatability. Among the different nanoformulations, the linear relationships were analyzed between the two variables using correlation matrices. Fe/MSU-F, Fe/MSU-F-NH$_2$, Mesocarbon, ZIF-8, and Mesobeta showed a positive relationship, while Fe/S-16/ZIF-8 exhibited a different correlation than the other groups (Tables 1 and S2†). The study shows excellent repeatability with no significant changes between the release time and between the groups (Table S1†). The Pearson correlation showed that Fe/

S-16/ZIF-8 exhibits a different behavior in comparison to the five other groups, clearly indicating the excellent Cp release under *in vitro* conditions (Table 1).

In order to understand the characteristics of the nanoformulations (ZIF-8, Fe/S-16 and Fe/S-16/ZIF-8), their physicochemical properties were analyzed. Fig. 3A–D shows the X-ray diffraction patterns (phase), FT-IR spectra (functional group), nitrogen isotherms (textural characteristics) and vibrating sample magnetometer plots (VSM). The X-ray diffraction spectrum of Fe/S-16 showed a broad peak due to the amorphous siliceous framework between 15–30°. The presence of weak diffraction peaks was observed, corresponding to the cubic structure of Fe$_3$O$_4$ (magnetite, PDF card # 88-0866) and γ-Fe$_2$O$_4$. The presence of such weak peaks with increased broadness is consistent with the presence of nanosized Fe$_3$O$_4$ inside the cubic cage nanopores of SBA-16 (nanocarriers). In the case of Fe/S-16/ZIF-8, the less intense peaks of ZIF-8 clearly show the transformation of crystalline ZIF-8 into a nanocomposite with SBA-16. Fig. 3B shows the nitrogen adsorption isotherm of Fe/SBA-16 and Fe/S-16/ZIF-8, respectively. The parent SBA-16 has a typical spinodal hysteresis pattern for the ink bottle-shaped pores with high surface area of 988 m$^2$ g$^{-1}$. The pore volume of SBA-16 was 0.69 cm$^3$ g$^{-1}$ with an average pore diameter of 3.3 nm. After iron oxide impregnation, the specific surface area decreased significantly to 471 m$^2$ g$^{-1}$, while the cumulative surface area reduced from 590 m$^2$ g$^{-1}$ to 297 m$^2$ g$^{-1}$ (Table 1). The observed reduction is about 50% after iron oxide impregnation. The cumulative pore volume of 0.37 cm$^3$ g$^{-1}$ showed a similar occupation (46%) when compared to that of the parent S-16. After composite formation with ZIF-8, the sample Fe/S-16/ZIF-8 showed a further reduction in the surface area to 365 m$^2$ g$^{-1}$ and pore volume to 0.33 cm$^3$ g$^{-1}$, which shows the deposition of ZIF-8 at the external surface of cubic caged SBA-16.

**Table 1** Correlation matrix of five different nanoformulations[a]

|  |  | Fe/MSU-F | Fe/MSU-F-NH$_2$ | Fe/Mesocarbon | ZIF-8 | Mesobeta | Fe/S-16/ZIF-8 |
|---|---|---|---|---|---|---|---|
| Fe/MSU-F | Pearson correlation | 1 | 0.915** | 0.823** | 0.878** | 0.108 | −0.511* |
|  | Sig. (2-tailed) |  | 0.000 | 0.000 | 0.000 | 0.670 | 0.030 |
|  | N | 18 | 18 | 18 | 18 | 18 | 18 |
| Fe/MSU-F-NH$_2$ | Pearson correlation | 0.915** | 1 | 0.869** | 0.765** | −0.095 | −0.694** |
|  | Sig. (2-tailed) | 0.000 |  | 0.000 | 0.000 | 0.707 | 0.001 |
|  | N | 18 | 18 | 18 | 18 | 18 | 18 |
| Fe/Mesocarbon | Pearson correlation | 0.823** | 0.869** | 1 | 0.690** | 0.037 | −0.707** |
|  | Sig. (2-tailed) | 0.000 | 0.000 |  | 0.002 | 0.886 | 0.001 |
|  | N | 18 | 18 | 18 | 18 | 18 | 18 |
| ZIF-8 | Pearson correlation | 0.878** | 0.765** | 0.690** | 1 | 0.340 | −0.247 |
|  | Sig. (2-tailed) | 0.000 | 0.000 | 0.002 |  | 0.167 | 0.324 |
|  | N | 18 | 18 | 18 | 18 | 18 | 18 |
| Mesobeta | Pearson correlation | 0.108 | −0.095 | 0.037 | 0.340 | 1 | 0.274 |
|  | Sig. (2-tailed) | 0.670 | 0.707 | 0.886 | 0.167 |  | 0.271 |
|  | N | 18 | 18 | 18 | 18 | 18 | 18 |
| Fe/S-16/ZIF-8 | Pearson correlation | −0.511* | −0.694** | −0.707** | −0.247 | 0.274 | 1 |
|  | Sig. (2-tailed) | 0.030 | 0.001 | 0.001 | 0.324 | 0.271 |  |
|  | N | 18 | 18 | 18 | 18 | 18 | 18 |

[a] **Correlation is significant at the 0.01 level (2-tailed). *Correlation is significant at the 0.05 level (2-tailed).
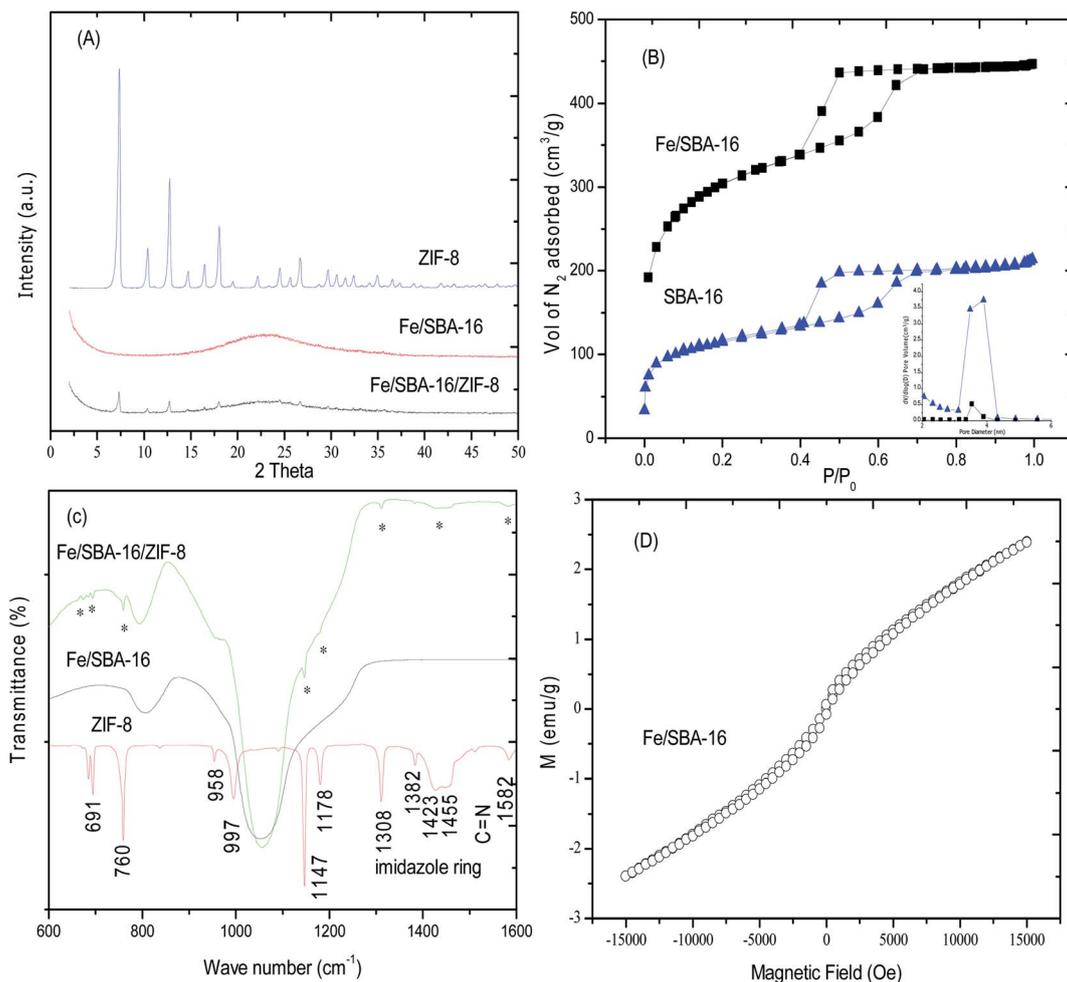
Fig. 3 Textural characterization of ZIF-8, Fe/S-16 and Fe/S-16/ZIF-8 using (A) X-ray diffraction (XRD), (B) $N_2$-adsorption isotherms, (C) Fourier-transformed infrared (FTIR) spectra and (D) vibrating sample magnetometry (VSM) analysis.

The FT-IR spectra of ZIF-8, Fe/SBA-16 and Fe/S-16/ZIF-8 are shown in Fig. 3C. ZIF-8 showed sharp stretching vibration peaks at 1582 $cm^{-1}$, 1147 $cm^{-1}$ and 997 $cm^{-1}$ due to the C=N and C–N groups. The presence of the imidazole ring was associated with the stretching bands at 1382 $cm^{-1}$, 1423 $cm^{-1}$ and 1455 $cm^{-1}$, respectively. The associated in-plane and out-of-plane bands were clearly observed at 1308 $cm^{-1}$, 1178 $cm^{-1}$, 958 $cm^{-1}$, 760 $cm^{-1}$ and 691 $cm^{-1}$, respectively. The spectrum of Fe/SBA-16/ZIF-8 showed the presence of characteristic ZIF-8 peaks, which indicates that nanosized ZIF-8 are present in correlation with the XRD and TEM analysis (Fig. 3A and 11). The presence of a similar pattern between the pure form of SBA-16 shows the retainment of the cubic structured SBA-16 that is maintained in the Fe/SBA-16/ZIF-8 composite. The introduction of 10 wt% iron oxide into the 3D pores of SBA-16 was measured for the magnetic behavior using VSM (Fig. 3D). The super paramagnetic behavior with a saturated magnetization of 2.39 emu $g^{-1}$ was observed. Such a pattern indicates that the iron oxide successfully transformed into nanoclusters in the thick pores of SBA-16.

The iron oxide coordination environment in the samples was further characterized using diffuse reflectance spectroscopy (Fig. S1†). The magnetic moments in SPIONs is due to the unpaired electrons in $Fe^{3+}$ and $Fe^{2+}$ species.[20] In the case of pure ZIF-8, the pristine form showed an intense characteristic peak absorbance at about 225 nm (Fig. S1a†). Iron oxide-impregnated SBA-16 (Fig. S1b†) showed an absorption band below 300 nm indicating the presence of tetrahedrally coordinated $Fe^{3+}$ species ($t_1$–$t_2$ and $t_1$–e).[21] The presence of a broadened absorption peak between 490–500 nm is attributed to the $O_2$ to $Fe^{3+}$ charge transfer. It has also been reported that the presence of dimeric $Fe^{2+}$ species results in a broad band between 328–389 nm.[22] The nanocomposite Fe/SBA-16/ZIF-8 showed a broad intermediate absorbance between Fe/SBA-16 and ZIF-8. The presence of a band at 375 nm indicates the presence of $Fe^{2+}$ ions coexisting with $Fe^{3+}$, thereby contributing to the magnetic moments. In addition, the presence of an elongated band between 300–700 nm for Fe/SBA-16/ZIF-8 shows the presence of aggregated forms of iron oxide (Fig. S1c†).
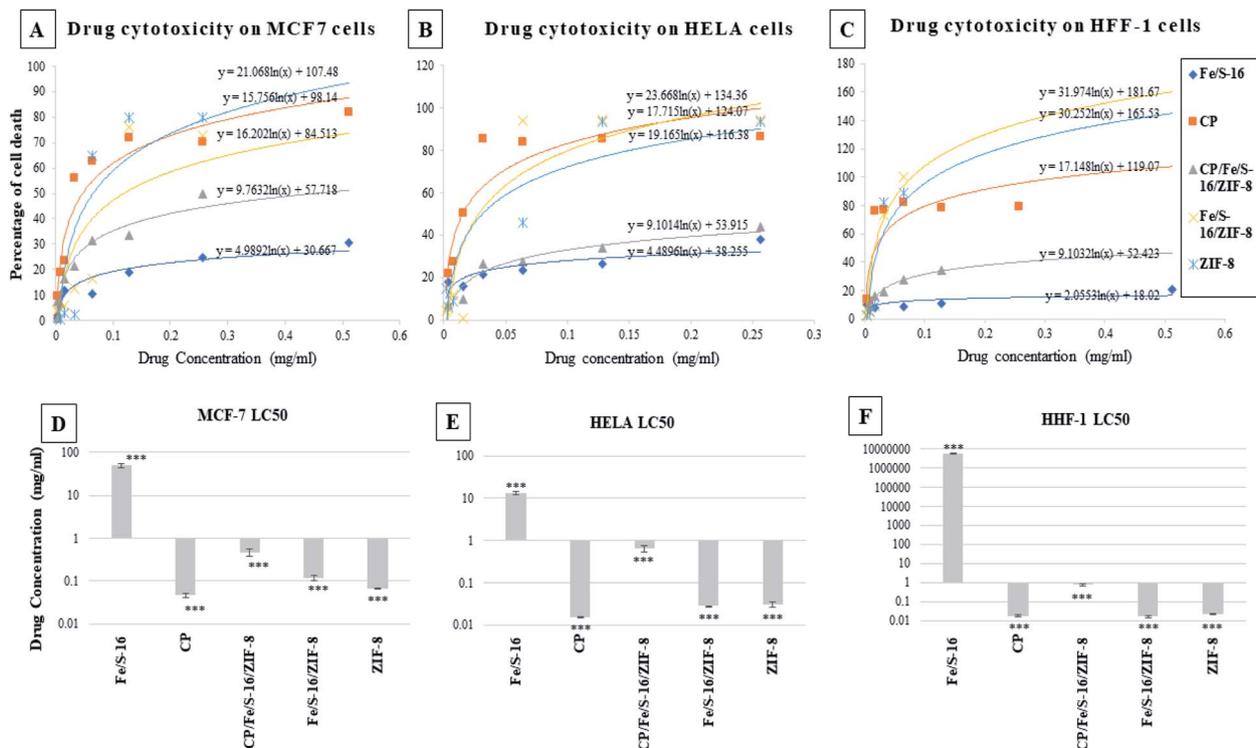
Fig. 4 Cytotoxicity effect of cisplatin, Fe/S-16, CP/Fe/S-16/ZIF-8, Fe/S-16/ZIF-8 and ZIF-8 on normal and cancer cell lines. (A) Breast cancer cell line MCF-7, (B) HeLa cervical cell line, and (C) normal cell lines HFF-1. $LC_{50}$ values for each of the drugs tested on the cell lines (D) MCF-7, (E) HELA and (F) HFF-1.

## 4.1. *In vitro* anti-cancer studies

The cytotoxicity study of Fe/S-16, cisplatin, CP/Fe/S-16/ZIF-8, Fe/S-16/ZIF-8 and ZIF-8 was performed on normal and cancer cell lines, as shown in Fig. 4: (A) breast cancer cell line MCF-7, (B) HeLa cervical cell line, and (C) normal cell lines HFF-1. These graphs were plotted to obtain $LC_{50}$ values for each of the drugs tested on the cell lines (refer to Table 2). Different concentrations of each nanoformulated drug and control were applied on each cell line; then, the cytotoxicity was measured by the MTT assay. The resulting data were plotted in excel and the $LC_{50}$ was calculated using the equation of the logarithmic trendline. The $p$ value and standard deviation were measured by a one-way ANOVA in GraphPad prism software plotting the $LC_{50}$ of the effective nanoparticles against the three cell lines (D) MCF-7, (E) HeLa and (F) HFF-1, ($***p < 0.001$, $n = 3$). These data show that

Fe/S-16/ZIF-8 and ZIF-8 are very toxic to the cancer cells in comparison to the control, and in some cell lines, Fe/S-16/ZIF-8 is more effective than cisplatin.

Light microscopy images were recorded for treated MCF-7, HeLa and HFF-1 with (A) cisplatin, (B) ZIF-8, (C) Fe/S-16/ZIF-8, (D) CP/Fe/S-16/ZIF-8, and (E) Fe/S-16 (Fig. 5–7). The images were ordered according to the reduction in the cell toxicity of each drug from A to E, at a concentration of 0.065 mg mL$^{-1}$, 0.032 mg mL$^{-1}$ and 0.016 mg mL$^{-1}$, respectively. The black debris is the dead cells and the brownish complex is the nanoparticles. Fe/S-16 treatment showed almost no effect in all the cell lines (Fig. 5–7), but $LC_{50}$ was varied between cell lines and was very high in normal cells HFF-1, moderate in MCF-7 and low in HeLa cells (Fig. 4, Table 2), indicating that the HeLa cells are the most sensitive cell line to Fe/S-16 followed by MCF-7 and then HFF-1.

Table 2  $LC_{50}$ of MCF-7, HeLa and HFF-1 treated with Fe/S-16, cisplatin, CP/Fe/S-16/ZIF-8, Fe/S-16/ZIF-8 and ZIF-8

| Drug | MCF-7 | | | HeLa | | | Human foreskin fibroblast | | |
|------|-------|-|-|------|-|-|---------------------------|-|-|
| | $LC_{50}$ (mg ml$^{-1}$) | $P$ value | SD | $LC_{50}$ (mg ml$^{-1}$) | $P$ value | SD | $LC_{50}$ (mg ml$^{-1}$) | $P$ value | SD |
| Fe/S-16 | 48.181 | 0.0003 | 5.294 | 13.682 | $3.08 \times 10^{-5}$ | 1.240 | 5721675.8 | $1.2908 \times 10^{-7}$ | 234268.1 |
| CP | 0.047 | 0.0003 | 0.005 | 0.015 | $3.08 \times 10^{-5}$ | 0.000 | 0.018 | $1.2908 \times 10^{-7}$ | 0.002 |
| CP/Fe/S-16/ZIF-8 | 0.454 | $2.1 \times 10^{-5}$ | 0.088 | 0.650 | $2.44 \times 10^{-6}$ | 0.106 | 0.766 | $1.2908 \times 10^{-7}$ | 0.135 |
| Fe/S-16/ZIF-8 | 0.119 | $2.0 \times 10^{-5}$ | 0.016 | 0.028 | $1.91 \times 10^{-6}$ | 0.001 | 0.016 | $1.2908 \times 10^{-7}$ | 0.003 |
| ZIF-8 | 0.065 | $2.0 \times 10^{-5}$ | 0.002 | 0.031 | $1.91 \times 10^{-6}$ | 0.005 | 0.022 | $1.2908 \times 10^{-7}$ | 0.001 |
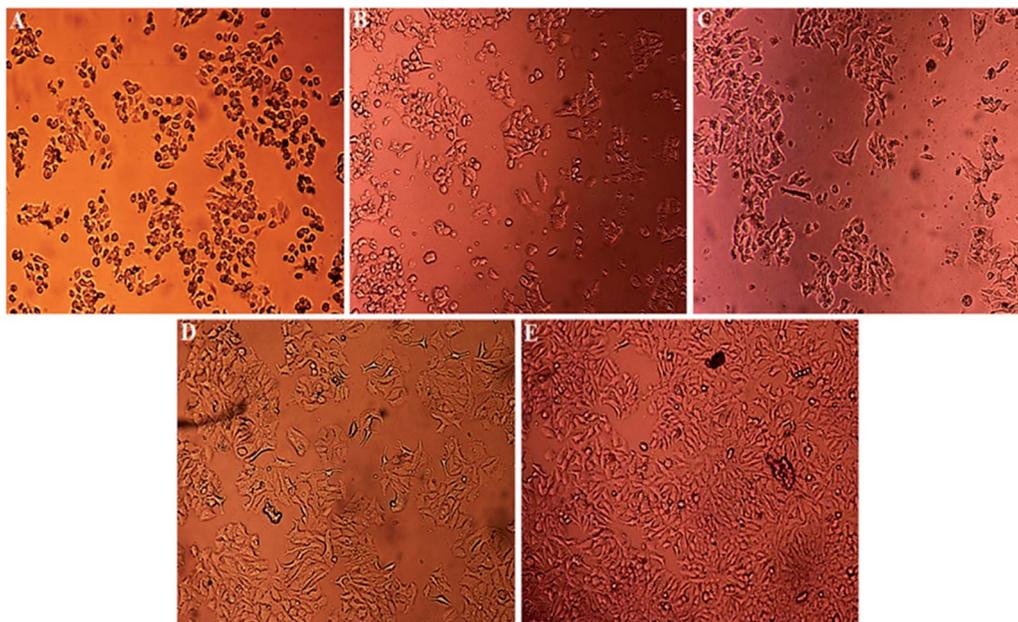
**Fig. 5** Light microscopy images of treated MCF-7 at a concentration of 0.065 mg mL$^{-1}$ with (A) cisplatin, (B) ZIF-8, (C) Fe/S-16/ZIF-8, (D) CP/Fe/S-16/ZIF-8, and (E) CP/Fe/S-16. The black debris is the dead cells and the brownish complex is the nanoparticles.

On the other hand, CP/Fe/S-16/ZIF-8, Fe/S-16/ZIF-8 and ZIF-8 showed high activity in cell killing compared to Fe/S-16, but less toxicity when compared to cisplatin. MCF-7 cells treated with CP/Fe/S-16/ZIF-8, Fe/S-16/ZIF-8, and ZIF-8 showed less toxicity than cisplatin by 9.6-fold, 2.52-fold and 1.39-fold, respectively. However, HeLa cells showed high sensitivity to Fe/S-16/ZIF-8 (1.85-fold less than CP) and more resistance to ZIF-8 and CP/Fe/S-16/ZIF-8, which were 2.0-fold and 42.56-fold compared to cisplatin. In HFF-1, the Fe/S-16/ZIF-8 activity was approximately the same as cisplatin and even little bit higher. Also, HFF-1 was more sensitive to ZIF-8, but it was less sensitive than cisplatin by 1.23-fold and more resistant to CP/Fe/S-16/ZIF-8 by 43.1-fold in comparison to cisplatin. CP/Fe/S-16/ZIF-8 was more active in MCF-7 than in HeLa and HFF-1 by 1.43-fold and 1.7-fold, respectively. HFF-1 was the most sensitive to Fe/S-16/ZIF-8 than HeLa and MCF-7 by 1.74-fold and 7.3-fold, respectively. In addition, ZIF-8 was the most toxic to HFF-1 cells in comparison to HeLa and MCF-7 by 1.42-fold and 2.97-fold, respectively. Overall, HFF-1 is the most sensitive toward Fe/S-16/ZIF-8 and ZIF-8 followed by HeLa and then MCF-7 and most resistant to CP/Fe/S-16/
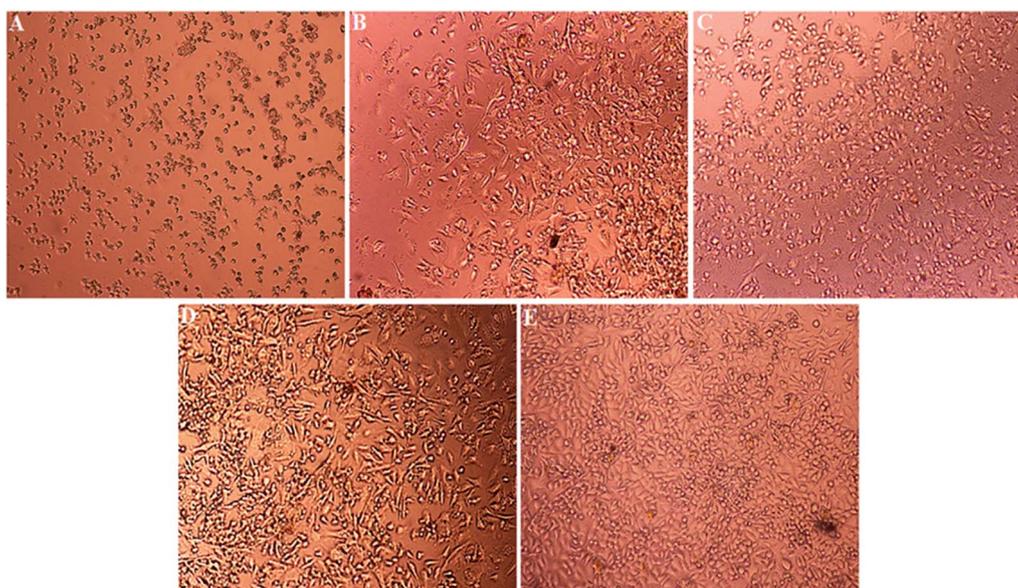


**Fig. 6** Light microscopy images of treated HeLa at a concentration of 0.032 mg mL$^{-1}$ with (A) cisplatin, (B) Fe/S-16/ZIF-8, (C) ZIF-8, (D) CP/Fe/S-16/ZIF-8, and (E) Fe/S-16. The black debris is the dead cells and the brownish complex is the nanoparticles.

**Fig. 7** Light microscopy images of treated HFF-1 at a concentration of 0.016 mg mL$^{-1}$ with (A) cisplatin, (B) Fe/S-16/ZIF-8, (C) ZIF-8, (D) CP/Fe/S-16/ZIF-8, and (E) CP/Fe/S-16. The images were ordered according to the reduction in cell toxicity of each drug from (A) to (E) respectively. The black debris is the dead cells and the brownish complex is the nanoparticles.

ZIF-8 followed by HeLa and MCF-7. Fe/S-16/ZIF-8, ZIF-8 and CP/Fe/S-16/ZIF-8 are highly toxic in all cell lines compared to the negative control Fe/S-16 (Fig. 4–7 and Table 2).

The confocal microscopy pictures of treated MCF-7, HeLa and HFF-1 (Fig. 8–10) confirmed that Fe/S-16/ZIF-8 and ZIF-8 showed a reduction in the cell numbers and are as effective as free drug cisplatin. The presence of CP in the CP/Fe/S-16/ZIF-8

formulation showed a reduction in the toxicity of the imidazole linker. The nuclear fragmentation and cell number reduction are slightly less than Fe/S-16/ZIF-8 and ZIF-8 but are higher than the negative control Fe/S-16. Fe/S-16/ZIF-8 and ZIF-8 showed DNA condensation, nuclear fragmentation and apoptotic bodies in the cells after treatment, indicating the high toxicity of these nanoformulated particles. The entry of CP/Fe/S-16/ZIF-8
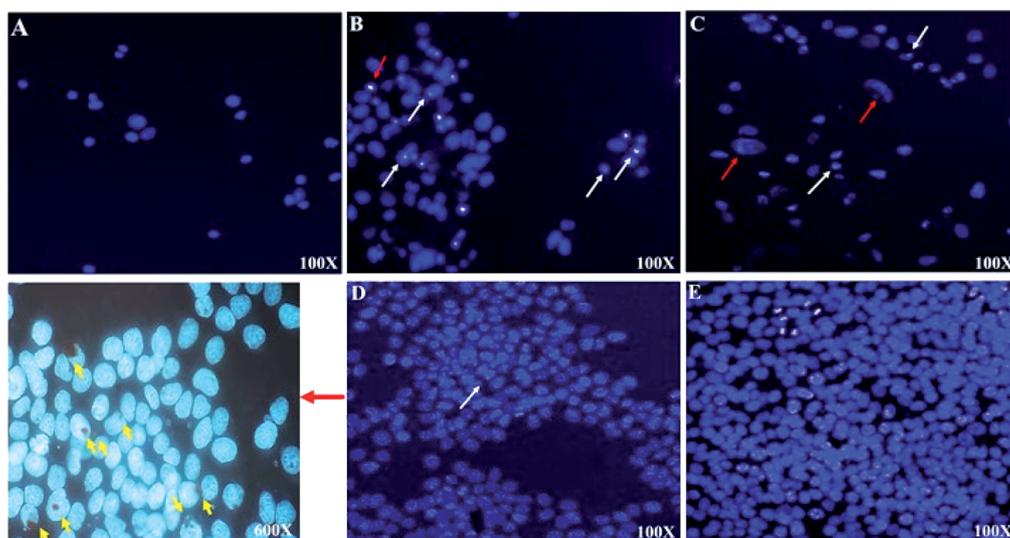


**Fig. 8** Hoechst staining of treated MCF-7 cells, the density stained areas are cell nuclei (blue color). (A) Cisplatin treatment (positive control) (0.065 mg mL$^{-1}$), Hoechst staining showing that the nuclei of the cisplatin treated cells are condensed, (B) Fe/S-16/ZIF-8 treatment (0.065 mg mL$^{-1}$), (C) ZIF-8 treatment (0.065 mg mL$^{-1}$), (D) CP/Fe/S-16/ZIF-8 treatment (0.065 mg mL$^{-1}$), higher magnification (600×) was taken using a semrock filter to show the cell entry and the red color of CP/Fe/S-16/ZIF-8, (E) CP/Fe/S-16 treatment (negative control) (0.065 mg mL$^{-1}$). The arrows indicate the nucleus structural changes. White arrow: DNA condensation. Red arrow: nuclear fragmentation/apoptotic bodies. Yellow arrows indicate the entry of CP/Fe/S-16/ZIF-8 (red particles) into the cells.
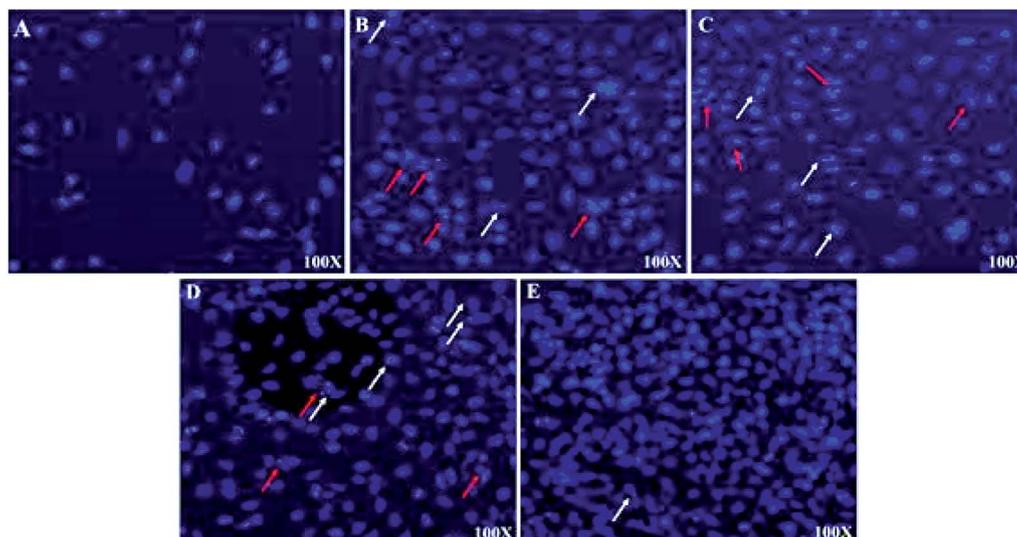
**Fig. 9** Hoechst staining of treated HeLa cells, the density stained areas are cell nuclei (blue color). (A) Cisplatin treatment (positive control) (0.028 mg mL$^{-1}$), Hoechst staining showing that cisplatin treated cells are at the final stage of apoptosis, (B) Fe/S-16/ZIF-8 treatment (0.028 mg mL$^{-1}$), (C) ZIF-8 treatment (0.028 mg mL$^{-1}$), (D) CP/Fe/S-16/ZIF-8 treatment (0.028 mg mL$^{-1}$), (E) Fe/S-16 treatment (negative control) (0.028 mg mL$^{-1}$). The arrows indicate the nucleus structural changes. White arrow: DNA condensation. Red arrow: nuclear fragmentation/apoptotic bodies.

in MCF-7 (yellow arrow, red particles, Fig. 8) was observed, demonstrating the possibility of these nanoformulated particles to be used for cell diagnosis and delivery.

The textural characteristics of a dry sample of Fe/S-16/ZIF-8 was analyzed through SEM-EDX (Fig. 11a–e) and TEM (Fig. 11f). The nanocomposite using SEM showed the presence of irregularly shaped crystals. The EDX pattern of the specimen shows the presence of Fe, Si, O, Zn, Pt and Cl, where Si and O are from the SBA-16 support. The pattern clearly shows the well-dispersed Fe and Zn of ZIF-8 and the Pt of cisplatin over the

SBA-16 support. In the TEM analysis of the dry sample, the presence of SPIONs as agglomerated nanoclusters was clearly observed over SBA-16 (Fig. 11f). The nanometer sized Fe$_3$O$_4$ and goethite (α-FeOOH) ranging between 10–15 nm were found to be interrelated with SBA-16 (Fig. S2†). The Fe$_3$O$_4$ nanoparticles with a $d$-spacing of 0.25 nm were microscopically captured with high dispersion over the SBA-16 support. ZIF-8 with sizes ranging to about 100 nm was observed as a composite with SBA-16. In the case of ZIF-8, zinc nanoparticles with a $d$-spacing of 0.21 nm were found to coexist with SPION nanoclusters
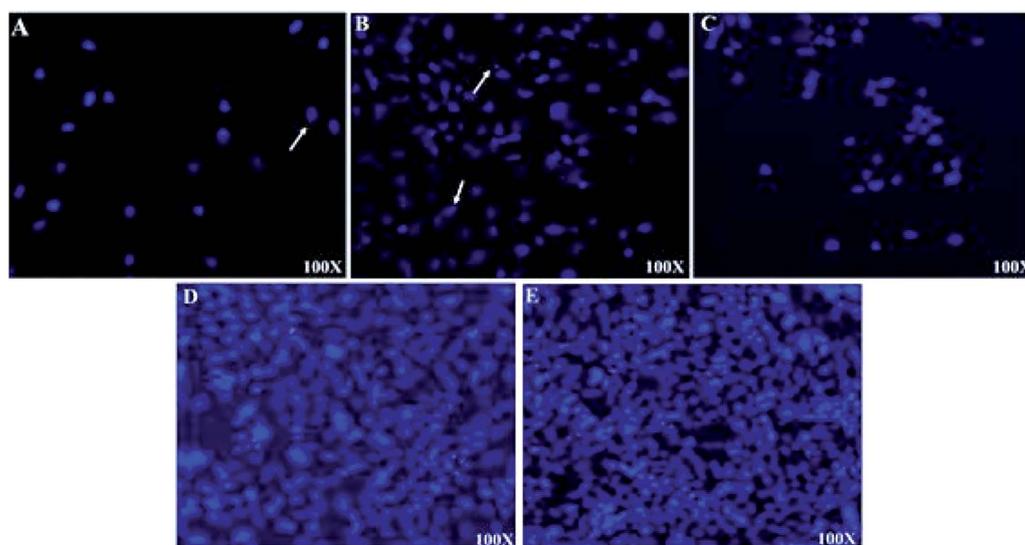


**Fig. 10** Hoechst staining of treated HFF-1 cells, the density stained areas are cell nuclei (blue color). (A) Cisplatin treatment (positive control) (0.016 mg mL$^{-1}$), (B) Fe/S-16/ZIF-8 treatment (0.016 mg mL$^{-1}$), (C) ZIF-8 treatment (0.016 mg mL$^{-1}$), (D) CP/Fe/S-16/ZIF-8 treatment (0.016 mg mL$^{-1}$), (E) Fe/S-16 treatment (negative control) (0.016 mg mL$^{-1}$). The arrows indicate the nucleus structural changes. White arrow: DNA condensation.
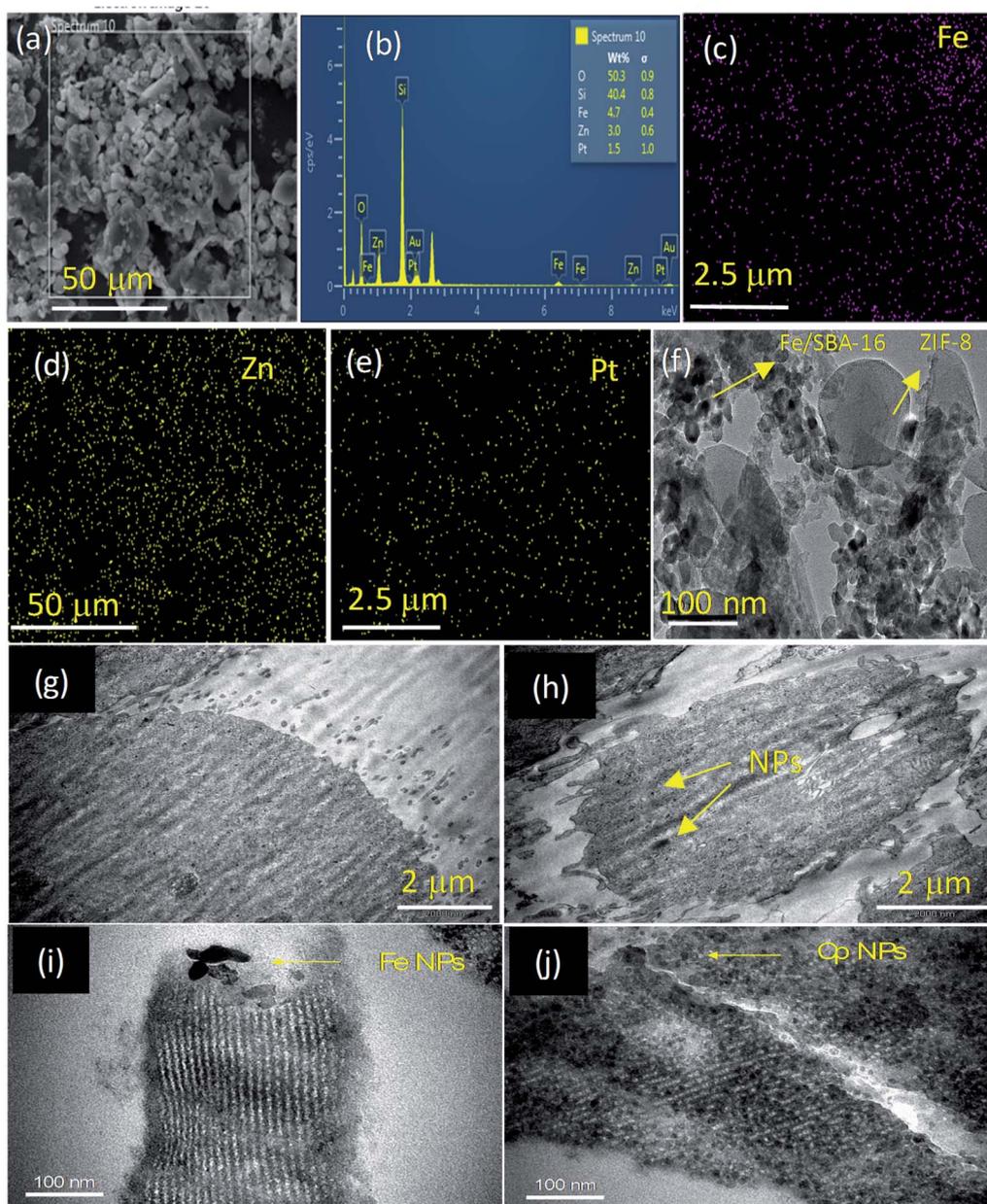
**Fig. 11** Morphology characterization using SEM–EDX and TEM. (a–e) SEM–EDX analysis of dry sample CP/Fe/SBA-16/ZIF-8, (f) TEM images of dry sample Fe/S-16/ZIF-8, (g–j) control (MCF-7) and CP/Fe/SBA-16/ZIF-8 treated MCF-7 cells examined by Bio-TEM at 100 nm scale bar (images were taking from ultramicrotomy sections having CP/Fe/S-16/ZIF-8 and cells).

(Fig. S2†). The morphology effects of the control (MCF-7) and CP/Fe/SBA-16/ZIF-8 treated MCF-7 cells were analyzed by Bio-TEM (Fig. 11g–j). The MCF-7 cell membrane (control) showed smooth and normal characteristics and morphology (Fig. 11g). However, the nanoformulation treated MCF-7 cells showed a non-uniform and damaged cell wall. The nanoparticle intrusion was clearly observed to lead to structural disintegration and cell death (Fig. 11h and S3†). The nanoformulation, CP/Fe/SBA-16/ZIF-8, in a saline environment (*e.g.* isotonic conditions) is shown at a higher magnification of 100 nm (Fig. 11i and j). A broad view of the TEM image shows the pore channels of the silica support, S-16. The SPIONs (Fe NPs) are deposited around the pore walls of the support, indicating that the Fe NPs possess both stability and uniform distribution over time in biological media (Fig. 11i). Furthermore, a good distribution of cisplatin nanoparticles was observed over S-16 (Fig. 11j). TEM analysis shows the differential distribution of both Fe and cisplatin nanoparticles over the silica support, thus highlighting the stability of the nanoformulation, CP/Fe/S-16/ZIF-8.

### 4.2. Minimal inhibitory concentration (MIC)

The MICs values of four nanoformulations; Ti-silicalite, Zn-silicalite, ZIF-8 and Fe/SBA-16/ZIF-8 were determined against methicillin-resistant *Staphylococcus aureus* (MRSA) and *P.*

*aeruginosa* (Table 3). Compound ZIF-8 and Fe/SBA-16/ZIF-8 had the lowest MIC values, *i.e.*, 625 and 1250 μg mL$^{-1}$, while compounds Ti-silicalite and Zn-silicalite had a greater MIC value *i.e.*, 2500 μg mL$^{-1}$ against *P. aeruginosa* and MRSA, respectively. Table 3 clearly shows that ZIF-8 and Fe/SBA-16/ZIF-8 (MIC 62.5–1250 μg mL$^{-1}$) possess better antibacterial activity than Zn-silicalite and Ti-silicalite (MIC 2500 μg mL$^{-1}$).

### 4.3. Inhibition of biofilm formation

The antibiofilm activity of four nanoformulations was investigated against biofilm forming strains of drug resistant *P. aeruginosa* and MRSA by a microtiter tissue culture plate assay. Fig. 12 clearly shows that all the tested compounds inhibit biofilm formation in a dose-dependent manner. Fe/SBA-16/ZIF-8 and ZIF-8 showed a maximum reduction of 83.59% and 73.48% against *P. aeruginosa* biofilms and 76.47% and 71.97% against MRSA biofilms, respectively, at 1000 μg mL$^{-1}$. Meanwhile, Zn-silicalite and Ti-silicalite inhibit the biofilm-forming ability of *P. aeruginosa* by 61.1% and 70.46% and MRSA by 67.1 and 67.7%, respectively, at similar doses (Fig. 8). From Fig. 10, it is very clear that Fe/SBA-16/ZIF-8 and ZIF-8 suppressed *P. aeruginosa* and MRSA biofilm formation more effectively than Zn-silicalite and Ti-silicalite.

MOFs have been reported as drug delivery systems for the release of 6-mercaptopurine,[23] 5-fluorouracil,[24] and tumor imaging agents.[25] MOFs are microporous in character and have been limited by their low mechanical and chemical stability.[26] The introduction of structured silica as a nanocomposite with MOFs was reported to improve the stability of MOFs. Hu *et al.*[27] reported a single step ZIF-8/silica composite with a disordered mesoporous structure. The composite involving ZIF-8/UVM-7 was found to be the best adsorbent material compared to ZIF-8/MCM-41 and ZIF-8/SBA-15 hybrids.[28] Gold incorporated mesoporous silica and ZIF-8 exhibit the plasmonic effect and dual types of pores originating from the triple hybrid nanoparticles (Au–SiO$_2$/MOF).[29] In the present study, iron oxide-impregnated 3D-structured SBA-16 silica was used as a nanocomposite with ZIF-8. The combination can improve the stability of ZIF-8 and can be used for dual applications (drug delivery and tumor imaging) in a single platform. 10 wt% Fe was loaded over siliceous S-16 through a forced impregnation technique. The presence of Fe$_3$O$_4$ with a crystalline cubic structure of magnetite and γ-Fe$_2$O$_3$ was confirmed through XRD. In addition, XRD shows
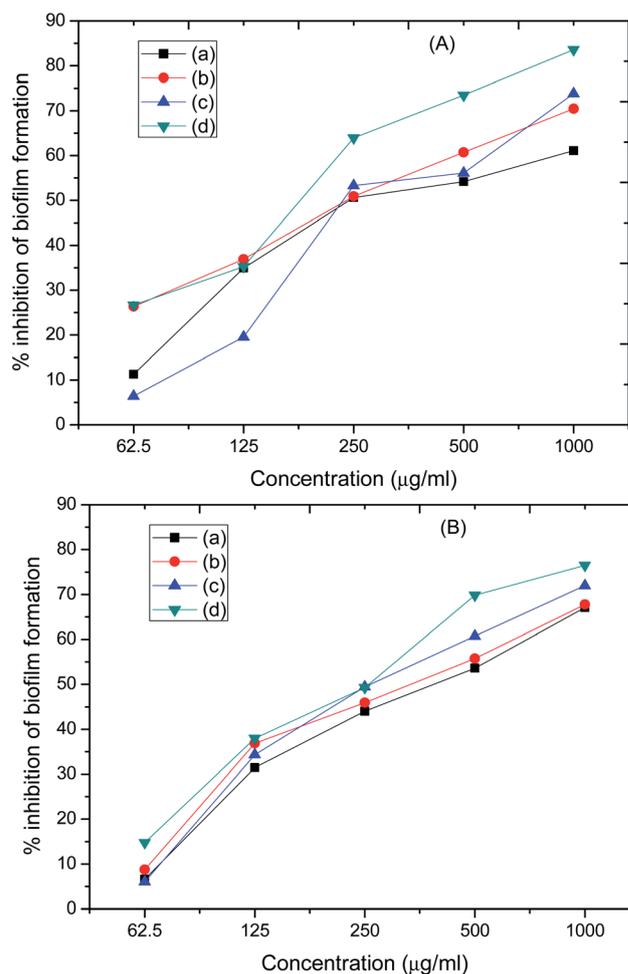
**Fig. 12** Effects of tested compounds (a) Ti-silicalite, (b) Zn-silicalite, (c) ZIF-8, and (d) Fe/SBA-16/ZIF-8 on biofilm formation abilities of (A) *P. aeruginosa* and (B) MRSA.

the successful transformation of ZIF-8 from crystalline to nanocomposite form (Fig. 3). The transformation of the poorly soluble drugs to nanosized carriers is reported to increase the bioavailability.[30] Therefore, the support SBA-16 in the present study is effective for transforming crystalline ZIF-8 to a nano-ZIF-8. The BET analysis further verifies the transition from microporous ZIF-8 to the mesoporous Fe/S-16/ZIF-8 composite (Fig. 3). TEM analysis shows the successful composite formation between ZIF-8 and S-16 that coexist with each other rather than as separate phases (Fig. 4). The Fe/SBA-16/ZIF-8 composite tends to exhibit high efficiency in cisplatin release compared to the parent ZIF-8 (Fig. 1 and 2). *In vitro* studies clearly show the anticancer effect of Fe/SBA-16/ZIF-8. In general, ZIF-8 composites are built with imidazole linkers and Zn$^{2+}$ species. Imidazole, an alkaloid, is reported to have phytochemical properties. Ali *et al.*[31] briefly mentioned the medical value of imidazole. Zn$^{2+}$ is reported to have antibacterial effects as well.[32] Therefore, the combination of nanosized Zn$^{2+}$ and heterocyclic imidazole present in Fe/SBA-16/ZIF-8 is proposed to act as an effective anticancer and antibacterial agent.

**Table 3** MIC (μg mL$^{-1}$) values of tested compounds against *P. aeruginosa* and MRSA

| MIC (μg mL$^{-1}$) | *P. aeruginosa* | MRSA |
|---|---|---|
| Ti-silicalite | 2500 | 2500 |
| Zn-silicalite | 2500 | 2500 |
| ZIF-8 | 1250 | 625 |
| Fe/SBA-16/ZIF-8 | 1250 | 1250 |

# 5. Conclusion

This study showed the anticancer and antibacterial properties of nanosized ZIF-8 in a Fe/S-16/ZIF-8 nanoformulation. Fe and ZIF-8 were impregnated in the matrix of three-dimensional SBA-16 through an impregnation and ultrasonication technique. The characterization analysis, including XRD and TEM, indicated the presence of nanosized $Fe_3O_4$, $\gamma$-$Fe_2O_4$ (magnetite) and $\alpha$-FeOOH (goethite) along with crystalline ZIF-8 as the composite with SBA-16. The magnetic analysis of Fe/SBA-16/ZIF-8 using vibrating-sample magnetometry exhibited paramagnetic behavior with a saturated magnetization value of 2.39 emu $g^{-1}$. The DRS-UV showed the co-existence of $Fe^{2+}$/$Fe^{3+}$ species on the surface of SBA-16, which contribute to the magnetic properties. The Fe/SBA-16/ZIF-8 activity was studied *in vitro* in MCF-7, HeLa cells and HFF-1 cells. The cumulative percentage of cisplatin drug release studied using an automated diffusion cell system showed that Fe/SBA-16/ZIF-8 has a higher release ability (75%) than that of Fe/S-16 (56%) and ZIF-8 (7.5%) over 72 h. The lethal concentration ($LC_{50}$) of Fe/SBA-16/ZIF-8 for MCF-7 and HeLa cells is 0.119 mg $mL^{-1}$ and 0.028 mg $mL^{-1}$ at 24 h, respectively. For HFF-1 cells, the $LC_{50}$ is 0.016 mg $mL^{-1}$. Cisplatin-containing Fe/SBA-16/ZIF-8 showed a concentration dependent inhibitory effect over MCF-7 in comparison to the HeLa and HFF-1 cells. Fe/SBA-16/ZIF-8 showed a high ability to transport drugs into the cytoplasm and induce cell death. ZIF-8 and Fe/SBA-16/ZIF-8 (MIC 62.5–1250 µg $mL^{-1}$) had better antibacterial activity than Zn-silicalite and Ti-silicalite (MIC 2500 µg $mL^{-1}$). The antibiofilm activity of Fe/SBA-16/ZIF-8 against biofilm-forming strains of drug resistant *P. aeruginosa* and MRSA showed the effective inhibition of biofilm formation in a dose-dependent manner. Overall, ZIF-8 exhibited a therapeutic effect due to the pharmacologically active imidazole linker. The paramagnetic Fe/SBA-16/ZIF-8 composite can be a potential candidate for magnetically driven cancer therapeutics and antibacterial and antibiofilm applications, which can be further manipulated with biocompatible polymers, natural antioxidants and large molecular anticancer drugs.

## Conflicts of interest

The authors declare no competing interests.

## Acknowledgements

## References

1 A. Phan, C. J. Doonan, F. J. Uribe-Romo, C. B. Knobler, M. O'Keeffe and O. M. Yaghi, *Acc. Chem. Res.*, 2010, **43**, 58–67, DOI: 10.1021/ar900116g.

2 Z. Ji, H. Zhang, H. Liu, O. M. Yaghi and P. Yang, *Proc. Natl. Acad. Sci. U. S. A.*, 2018, **115**(42), 10582–10587, DOI: 10.1073/pnas.1808829115.

3 S. R. Miller, D. Heurtaux, T. Baati, P. Horcajada, J.-M. Grenèche and C. Serre, *Chem. Commun.*, 2010, **46**, 4526–4528, DOI: 10.1039/C001181A.

4 Q. Zhao, J. Wang, Y. Zhang, J. Zhang, A. Tang and D. Kong, *J. Mater. Chem. B*, 2018, **6**, 7898, DOI: 10.1039/C8TB02663G.

5 H. Kaur, G. C. Mohanta, V. Gupta, D. Kukkar and S. Tyagi, *J. Drug Delivery Sci. Technol.*, 2017, **41**, 106–112, DOI: 10.1016/j.jddst.2017.07.004.

6 K. S. Park, Z. Ni, A. P. Cote, J. Y. Choi, R. Huang, F. J. Uribe-Romo, H. K. Chae, M. O'Keeffe and O. M. Yaghi, *Proc. Natl. Acad. Sci. U. S. A.*, 2006, **103**(27), 10186–10191, DOI: 10.1073/pnas.0602439103.

7 X. Yan, X. Hua and S. Komarnenib, *RSC Adv.*, 2014, **4**, 57501, DOI: 10.1039/c4ra09626f.

8 R. Saeedirad, S. T. Ganjali, M. Bazmi and A. Rashidi, *J. Taiwan Inst. Chem. Eng.*, 2018, **82**, 10–22, DOI: 10.1016/j.jtice.2017.10.037.

9 E. Perez-Esteve, M. Ruiz-Rico, R. Martinez-Manez and J. M. Barat, *J. Food Sci.*, 2015, **80**, E2504–E2516, DOI: 10.1111/1750-3841.13095.

10 T. Ohhashi, T. Tsuruoka, K. Inoue, Y. Takashima, S. Horike and K. Akamatsu, *Microporous Mesoporous Mater.*, 2017, **245**, 104–108, DOI: 10.1016/j.micromeso.2017.02.074.

11 L. Wang, Q. Teng, X. Sun, Y. Chen, Y. Wang, H. Wang and Y. Zhang, *J. Colloid Interface Sci.*, 2018, **512**, 127–133, DOI: 10.1016/j.jcis.2017.10.050.

12 T. Zhang, B. Li, X. Zhang, J. Qiu, W. Han and K. L. Yeung, *Microporous Mesoporous Mater.*, 2014, **197**, 324–330, DOI: 10.1016/j.micromeso. 2014.07.002.

13 A. Prabhu, A. AlShoaibi and C. Srinivasakannan, *Mater. Lett.*, 2015, **146**, 43–46, DOI: 10.1016/j.matlet.2015.01.156.

14 K. Higuchi and T. Yanagawa, *PLoS One*, 2019, **14**, e0215757, DOI: 10.1371/journal.pone.0215757.

15 B. Rabindran Jermy, M. Alomari, V. Ravinayagam, S. A. Almofty, S. Akhtar, J. Francis Borgio and S. AbdulAzeez, *Sci. Rep.*, 2019, **9**, 14523, DOI: 10.1038/s41598-019-51051-w.

16 B. Rabindran Jermy, S. Acharya, V. Ravinayagam, H. S. Alghamdi, S. Akhtar and R. S. Basuwaidan, *Appl. Nanosci.*, 2018, **8**, 1205, DOI: 10.1007/s13204-018-0786-9.

17 M. A. Ansari and M. A. Alzohairy, *J. Evidence-Based Complementary Altern. Med.*, 2018a, 1860280, DOI: 10.1155/2018/1860280.

18 K. Kalishwaralal, S. B. M. Kanth, S. R. K. Pandian, V. Deepak and G. Gurunathan, *Colloids Surf., B*, 2010, **79**, l340–344, DOI: 10.1016/j.colsurfb.2010.04.014.

19 H. Kaur, G. C. Mohanta, V. Gupta, D. Kukkar and S. Tyagi, *J. Drug Delivery Sci. Technol.*, 2017, **41**, 106–112, DOI: 10.1016/j.jddst.2017.07.004.

20 G. Kandasamy and D. Maity, *Int. J. Pharm.*, 2015, **496**, 191–218, DOI: 10.1016/j.ijpharm.2015.10.058.

21 N. S. Sanjini and S. Velmathi, *RSC Adv.*, 2014, **4**, 15381–15388, DOI: 10.1039/c3ra46303f.

22 S. Shwan, J. Jansson, L. Olssona and M. Skoglundha, *Catal. Sci. Technol.*, 2014, **4**, 2932–2937, DOI: 10.1039/c4cy00236a.

23 H. Kaur, G. C. Mohanta, V. Gupta, D. Kukkar and S. Tyagi, *J. Drug Delivery Sci. Technol.*, 2017, **41**, 106–112, DOI: 10.1016/j.jddst.2017.07.004.

24 C. Sun, C. Qin, X.-L. Wang, G.-S. Yang, K. Shao, Y.-Q. Lan, Z.-M. Su, P. Huang, C.-G. Wang and E.-B. Wang, *Dalton Trans.*, 2012, **41**, 6906–6909, DOI: 10.1039/c2dt30357d.

25 X. Gao, R. Cui, G. Jia and Z. Liu, *Nanoscale*, 2018, **10**, 6205–6211, DOI: 10.1039/C7NR08892B.

26 L. Ma, C. Abney and W. Lin, *Chem. Soc. Rev.*, 2009, **38**, 1248–1256, DOI: 10.1039/b807083k.

27 X. Hu, X. Yan, M. Zhou and S. Komarneni, *Microporous Mesoporous Mater.*, 2016, **219**, 311–316, DOI: 10.1039/b807083k.

28 R. Saeedirad, S. T. Ganjali, M. Bazmi and A. Rashidi, *J. Taiwan Inst. Chem. Eng.*, 2018, **82**, 10–22, DOI: 10.1016/j.jtice.2017.10.037.

29 T. Ohhashi, T. Tsuruoka, K. Inoue, Y. Takashima, S. Horike and K. Akamatsu, *Microporous Mesoporous Mater.*, 2017, **245**, 104–108, DOI: 10.1016/j.micromeso.2017.02.074.

30 K. E. Bremmell and C. A. Prestidge, *Drug Dev. Ind. Pharm.*, 2019, **45**, 349–358, DOI: 10.1080/03639045.2018.1542709.

31 I. Ali, M. N. Lone and H. Y. Aboul-Enein, *MedChemComm*, 2017, **8**, 1742–1773, DOI: 10.1039/c7md00067g.

32 S. Rehman, B. Rabindran Jermy, S. Akhtar, J. Francis Borgio, S. Abdul Azeez, V. Ravinayagam, R. A. Jindan, Z. H. Alsalem, A. Buhameid and A. Gani, *Artif. Cells, Nanomed., Biotechnol.*, 2019, **47**, 2072–2082, DOI: 10.1080/21691401.2019.1620254.